High-Speed Adaptive MIMO-VLC System with Neural Network

Fangxiao Dong, *Student Member, IEEE*, Dominic O'Brien, *Member, IEEE*

***Abstract*—Rooms are typically lit with multiple luminaires, which open the possibility of creating Multiple-Input Multiple-Output (MIMO) Visible Light Communications (VLC) systems. At its most complex, the luminaires in the system might transmit different data at different power levels to a terminal containing multiple receivers, allowing a substantial increase in data rates. However, crosstalk between the transmitted channels, dependent on the location and orientation of the receiver, may cause the best strategy to be to group transmitters together and transmit the same data stream. In this paper, we report a transmitter coordination algorithm determining how to use the transmitters optimally as the receiver location varies. The data rate using this approach is on average 41 per cent higher than the conventional spatial multiplexing approach. Neural networks are then employed in the coordination algorithm. It increases the speed of operation by a factor of four compared to the initial coordination algorithm while achieving the same level of performance. The neural network also gives good performance for room geometries and receiver orientations outside the scope of the training data. Finally, the neural network is benchmarked against a water-filling algorithm approach with maximum system capacity. The neural network shows a factor of three speed-up in computing time with only a 12 per cent reduction in the average data rate. These results show the potential of the approach to achieve a near-maximal data rate with a straightforward and efficient channel selection technique.**

***Index Terms*—Visible Light Communications (VLC), Multiple-Input Multiple-Output (MIMO), Angular Diversity Receiver, Transmitter Coordination, Artificial Neural Network (ANN)**

I. Introduction

Mobile data traffic has experienced exponential growth in recent decades, which imposes increasing pressure on the limited resources of wireless communications. Meanwhile, the increased use of white light-emitting diodes (LEDs) and the broad unlicensed spectrum of the optical wavelengths has led to a growing interest in a novel wireless technology: Indoor visible light communication (VLC). The unlicensed spectrum provided by VLC supplies the additional capacity to mobile communication systems, while the LEDs can also offer illumination. This illumination is often provided by multiple LEDs installed on the ceiling in an indoor environment, which offers the potential to develop Multiple-Input Multiple-Output (MIMO) VLC systems.

MIMO-VLC enables multiple wireless channels between multiple transmitters and receivers, bringing higher spectral efficiency and data transmission rates [1]. However, it also introduces challenges. First, multiple LEDs inside a room leads to multi-stream interference (MSI) between them. The decreased signal-to-interference-plus-noise ratio (SINR) caused by this interference degrades the system performance. Second, band-limited VLC channels bring inter-symbol interference (ISI) during high-speed communications. Third, the structure of the receiver affects the received interference and SINR of each channel. The work aims to best use the MIMO resources in a VLC system to achieve high data rate performance and low complexity in terms of control and implementation.

Spatial multiplexing (SMP), spatial modulation (SM) and ganging are common schemes employed in MIMO-VLC systems, each with its own attributes and disadvantages. With SMP, different transmitters carry different data sequences in parallel. SMP increases the spectral efficiency by a factor of the number of transmitters N_t (see, e.g., [2], [3]). However, multiple channels may also cause MSI between channels, reducing the practical improvement that can be achieved. SM typically uses one transmitter at a time and decides the index of the transmitter based on the transmitted data bits. In this case, the spectral efficiency of the channel can be improved by a factor of $log_2(N_t)$. Related works and variants of this scheme can be found in [4], [5] and [6]. In the case of ganging, all transmitters work together to send the same data stream. This does not improve spectral efficiency but improves the SINR of the channel. Ganging allows similar channels (which can have severe interference from each other) to be combined, thus making the best use of the impaired channels (see, e.g. [7], [8]).

Ideally, a receiver in VLC needs to have a large collection area and a wide field-of-view (FOV) [9], ensuring that as much optical power as possible can be collected. However, there is a trade-off between FOV and collection area due to the conservation of etendue [9]. This problem can be solved by using receiver designs with higher diversity. The spatial diversity receiver is one solution (see, e.g., [7]). However, in an intensity modulation direct detection (IM/DD) system such as this, the received signal power changes slowly by varying the receiver position [10], making it difficult to use spatial diversity to achieve well-conditioned MIMO channels. The angular diversity receiver is another solution (see, e.g., [11]–[13]). In this case, high diversity between channels can be achieved by pointing receivers to different directions and the goal of wide FOV and large collection area is met at the same time.

In [14], we proposed a new modulation scheme known as the channel condition-based transmitter coordination (CCTC) algorithm. The algorithm adaptively combines SMP and ganging to optimise the transmitter patterns and data rates based on the channel conditions, reducing the MSI and optimising the achievable data rates. An angular diversity receiver design is

also employed, bringing wide FOV and reduced spatial correlation among received signals.

Precoding is a common approach to reduce MSI in MIMO (or MISO) VLC systems. Reference [15] proposed a modulation precoding scheme that conducts adaptive power allocation on LEDs, maximising the minimum distance between received symbols and mitigating the MSI. In [16], the author used 4QAM and geometrically-shaped square 8QAM from two LEDs to superpose into 32QAM signals and addressed high channel correlation in SMP systems. A joint precoder and equaliser optimisation design are developed in [17]. The employment of this design improves the bit error rate (BER) of the system when taking into account the channel estimation imperfection. In the proposed work, the ganging of channels with high correlation achieves a similar reduction in MSI as precoding, allowing the zero-forcing equalisation employed in the system to achieve a good performance. The advantage of the proposed approach is that it is simple enough, as the average and modulated optical power of each LED is fixed, and any data routing required to gang channels can be achieved using simple digital multiplexers and switches.

In this paper, we investigate the use of artificial neural networks (ANNs) in order to keep mitigating the complexity of the MIMO-VLC system in [14]. ANNs are computing systems that roughly model how animal brains process information [18]. Work reported in [18] and [20] demonstrate the user positioning in the VLC systems with ANN estimation. References [21], [22] and [23] investigate the ANN-based physical layer techniques in the VLC systems, but to the best of our knowledge, there is no work applying an ANN to predict the transmitter patterns and data rates of a MIMO-VLC system.

The ANN approach described in this system builds on the work in [14] (which used exhaustive search) and presents new results that show:

1) ANNs are robust, and this work shows that they perform well even if the testing data falls outside the scope of the training data.
2) The computational complexity of the ANN-based system is three to four times lower than the CCTC algorithm-based one and three times lower than its benchmark: the water-filling algorithm.
3) The implementation and control of the ANN-based system are simpler than that of the water-filling algorithm with maximum system capacity.

Overall, the paper shows that the system operates over a wide range of conditions (incorporating a statistical model of human walking) with different room geometries, varying receiver positions and orientations.

The paper is organised as follows. Section II provides the VLC system model, including the angular diversity receiver design. Section III provides details about the CCTC algorithm and how it works. Section IV and section V demonstrates systems with ANNs to reduce the computational complexity of the CCTC algorithm. The ANN-based system is compared with the systems with the CCTC algorithm and the water-filling algorithm. Section VI gives a conclusion.

II. VLC System Model

The system model can be found in [14], and a summary of the description is given in this section. Fig. 1 shows a schematic of a typical indoor MIMO-VLC system, where N_t LEDs are installed on the ceiling of the room, and a receiver with N_r receiver elements (REs) is located on the receiver plane. The channels among N_t LEDs and N_r REs can be arranged in a $N_r \times N_t$ matrix, $\boldsymbol{H}$. The LEDs are assumed to be operated by a controller. The receiver is an angular diversity receiver with REs pointing in different directions. Each RE receives light from one or more LED(s) with different light intensities [24]. A schematic of the system model is given in Fig. 2. The parameters of the system are shown in Table I.

TABLE I
PARAMETERS

Parameters	Values
Room size (width × length × height)	5 m × 5 m × 3m
Receiver plane height	0.85 m
Numbers of LEDs (N_t)	4
Modulation power per LED (P_{LED})	1 W
LED pitch	2.5 m
Lambertian order (m)	1
LED and receiver bandwidth	8.4 MHz [24]
Collection area per RE (A_j)	100 mm^2
Half-angle FOV (β_c) per RE	33°
Detector responsivity (ρ)	0.4 A/W [24]
Pre-amplifier noise current density (i_{amp})	5 pA/Hz$^{1/2}$ [24]
Ambient light photocurrent density ($\gamma_{ambient}$)	10.93 A/(m^2·Sr) [25]

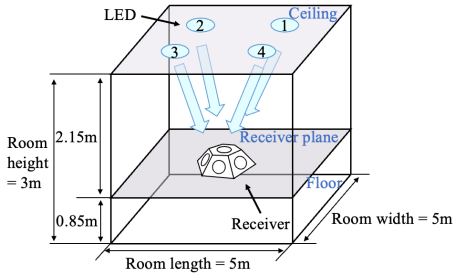

Fig. 1. Configuration of a typical indoor MIMO-VLC system.

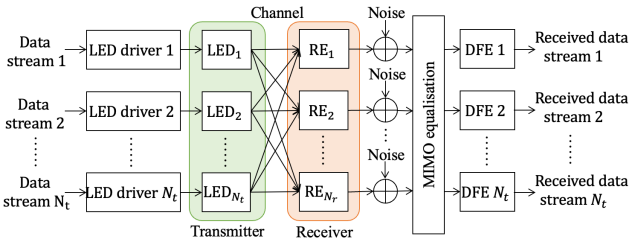

Fig. 2. Schematic of the indoor MIMO VLC system [14].

A. Transmitter

On the transmitter side, N_t white LEDs are placed on the ceiling to illuminate the room and offer communications. In this work, there are four LEDs arranged as a 2×2 array. A white LED source typically includes a blue LED and a yellow phosphor coating, and the slow time response of the yellow phosphor constrains the LED bandwidth to 2.5 MHz [24]. The bandwidth is improved by placing a blue filter on the RE to

make sure only the blue emission component of the LED is detected. The improved LED bandwidth is typically around 10 MHz to 20 MHz [26]. In this model, the LED bandwidth is set as 8.4 MHz, the same as the employed receiver bandwidth [24].

The LEDs use Non-Return to Zero On-Off Keying (NRZ-OOK) to modulate the data. A random binary data stream is generated and converted to a non-negative electrical signal. Then, the LED emits the signal by modulating it as different light intensities. The electrical signal is convolved with the impulse response of the LED [27]

$$h_{LED}(t) = e^{-\omega_c t}, \tag{1}$$

where ω_c is the 3dB cut-off frequency with angular frequency unit, which is also the bandwidth of the LED. Vector $\boldsymbol{D} = [d_1, \dots d_i \dots, d_{N_t}]^T$ represents the output of the LED at each time instant. d_i indicates the convolution of the ith data sequence and the impulse response of the ith LED. T means the transpose of a vector or a matrix.

B. VLC Channel

$N_r \times N_t$ MIMO channel matrix $\boldsymbol{H}$ is shown as

$$\boldsymbol{H} = \begin{bmatrix} h_{11} & \dots & h_{1i} & \dots & h_{1N_t} \\ \vdots & \ddots & \vdots & & \vdots \\ h_{j1} & \dots & h_{ji} & \dots & h_{11} \\ \vdots & & \vdots & \ddots & \vdots \\ h_{N_r1} & \dots & h_{N_ri} & \dots & h_{N_rN_t} \end{bmatrix}, \tag{2}$$

where h_{ji} indicates the DC gain from the ith LED to the jth RE. h_{ji} can be calculated from

$$h_{ji} = \begin{cases} \dfrac{(m+1)A_j}{2\pi {d_{ji}}^2} cos^m(\alpha_{ji}) cos(\beta_{ji}) \\ \qquad\qquad 0 \le \alpha_{ji} \le \dfrac{\pi}{2} and\ 0 \le \beta_{ji} \le \beta_c \\ 0 \qquad\qquad otherwise \end{cases}, \tag{3}$$

where m is the Lambertian source order, d_{ji} is the distance between the ith LED and the jth RE, A_j is the collection area of the jth RE, α_{ji} is the light irradiance angle of the ith LED in respect of the jth RE, β_{ji} is the incident angle of the jth RE in respect of the ith LED, and β_c is the half-angle FOV of the receiver. The system model only considers the line-of-sight (LOS) link.

Fig. 3 shows a geometry of a LED and RE pair [11]. $\overrightarrow{V_i}$ is the pointing direction of the i th LED, which is vertically downwards, $\overrightarrow{W_j}$ represents the pointing direction of the jth RE, $\overrightarrow{P_{ji}}$ is the vector pointing from the ith LED to the jth RE. α_{ji} and β_{ji} can be derived from $\overrightarrow{V_i}$, $\overrightarrow{W_j}$ and $\overrightarrow{P_{ji}}$, as shown in [11].

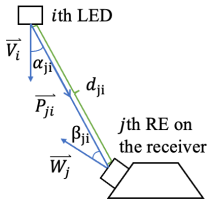

Fig. 3. Relative geometry between a LED and RE pair.

C. Receiver

A receiver with N_r REs is placed on the receiver plane. The signals detected by the REs at a time instant is

$$\boldsymbol{R} = \rho P_{LED}(\boldsymbol{H} \bullet \boldsymbol{D}) + \boldsymbol{i}_N, \tag{4}$$

where $\boldsymbol{R} = [r_1, \dots r_j \dots, r_{N_r}]^T$ and r_j indicates the electrical signal received by the jth RE at a time instant, ρ indicates detector responsivity converting the optical signal to the electrical signal, P_{LED} is the modulation power of each LED [24], $\boldsymbol{i}_N = [i_{n,1}, \dots i_{n,j} \dots, i_{n,N_r}]^T$ represents the noise current vector with $i_{n,j}$ as the noise of the jth RE at a time instant. The transmission rate of the blue filter is set as 100 per cent and is not shown in (4).

The noise of the RE includes the optical signal noise from the desired signal, the ambient noise from the ambient light and the amplifier noise from the pre-amplifier circuit [28]. $i_{n,j}$ is an independent identically distributed (i.i.d.) additive white Gaussian noise (AWGN) random variable [11]. The variance of it is derived from the mean square value of the noise

$$\overline{i_{n,j}^2} = 2e\left(i_{signal,j} + i_{ambient,j}\right)B + i_{amp}^2 B, \tag{5}$$

where e is the elementary charge, $i_{signal,j}$ is the mean noise current density received by the jth RE, $i_{ambient,j}$ and i_{amp} are the ambient light noise current density and the pre-amplifier noise current density, and B indicates the receiver bandwidth. The $i_{signal,j}$ is calculated as

$$i_{signal,j} = \rho P_{LED} \sum_{i=1}^{N_t} h_{ji}\, d_i, \tag{6}$$

The $i_{ambient,j}$ of the jth RE is derived from

$$i_{ambient,j} = \gamma_{ambient} A_j 2\pi(1 - \cos(\beta_c)), \tag{7}$$

where $\gamma_{ambient}$ is the ambient light photocurrent per square meter per steradian and $2\pi(1 - \cos(\beta_c))$ denotes the solid angle of a cone assigned to a cross-section having a $2\beta_c$ angle.

After that, the matrix is demultiplexed by a linear zero-forcing equaliser (ZFE). The estimation of the transmitted signal is

$$\widehat{\boldsymbol{D}} = \boldsymbol{H_{ZF}} \bullet \boldsymbol{R}, \tag{8}$$

where $\boldsymbol{H_{ZF}}$ is the Moore-Penrose inverse of the matrix $\boldsymbol{H}$

$$\boldsymbol{H_{ZF}} \stackrel{\text{def}}{=} (\boldsymbol{H}^*\boldsymbol{H})^{-1}\boldsymbol{H}^*, \tag{9}$$

where $\boldsymbol{H}^*$ is the conjugate transpose of $\boldsymbol{H}$.

D. Decision Feedback Equaliser

After demultiplexing, decision-feedback equalisers (DFEs) are employed to reduce ISI in the signals. Each channel (or channel group) has its DFE separately trained.

Fig. 4 shows a DFE structure established in the direct transversal form [29].

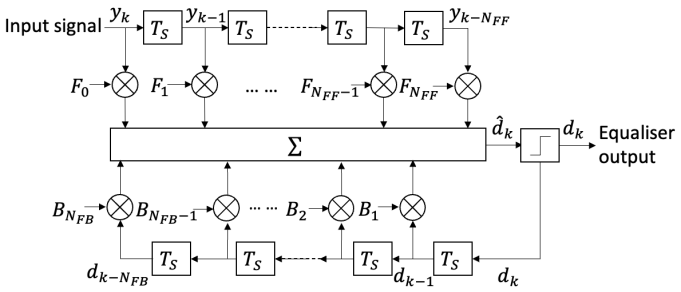

Fig. 4. Structure of the decision-feedback equaliser.

The DFE system consists of a transversal feed-forward filter and a transversal feedback filter. T_S is delay tap. The output of the system $\hat{d}_k$ is expressed as

$$\hat{d}_k = \sum_{m=0}^{N_{FF}} F_m(k) y_{k-m} + \sum_{n=1}^{N_{FB}} B_n(k) d_{k-n}\,, \tag{10}$$

where $\boldsymbol{F}_k = [F_0(k)\ F(k)_1 \dots F_{N_{FF}}(k)]$ are weighting coefficients for the feed-forward filter at time instant k and $\boldsymbol{B}_k = [B_1(k)\ B_2(k) \dots B_{N_{FB}}(k)]$ are weighting coefficients for the feed-back filter. $\boldsymbol{y}_k = [y_k\ y_{k-1} \dots y_{k-N_{FF}}]$ is the input signal to the equaliser. The previous decisions $d_{k-1}, d_{k-2} \dots d_{k-N_{FB}}$ are fed back into the DFE. d_k at time instant k can be obtained after making a decision on the detected signal $\hat{d}_k$.

DFE needs an algorithm to update the weighting coefficients $\boldsymbol{F}_k$ and $\boldsymbol{B}_k$ to their optimum values, and the least mean square (LMS) is employed here [29]. By using the LMS algorithm, the vector $\boldsymbol{F}_k$ and $\boldsymbol{B}_k$ are continuously updated in each iteration until the minimum mean square error (MSE) $e(k)$ is obtained, as shown below

$$\boldsymbol{W}_{k+1} = \boldsymbol{W}_k + \mu e(k) \boldsymbol{Y}_k\,, \tag{11}$$

where

$$\begin{aligned} \boldsymbol{W}_k &= [\boldsymbol{F}_k \boldsymbol{B}_k] \\ &= [F_0(k)F_1(k) \dots F_{N_{FF}}(k)\ B_1(k)B_2(k)\ \dots B_{N_{FB}}(k)]\,, \end{aligned} \tag{12}$$

$$\boldsymbol{Y}_k = [y_k\ y_{k-1}\ \dots\ y_{k-N_{FF}}\ d_{k-1}\ d_{k-2} \dots d_{k-N_{FB}}]\,, \tag{13}$$

and μ is the step size. $e(k)$ is the error

$$e(k) = d_{training,k} - \hat{d}_k\,, \tag{14}$$

where $d_{training,k}$ is the known training sequence transmitted through the equaliser. The error is calculated from the difference between the detected signal $\hat{d}_k$ and the known training sequence.

For each DFE, a known training data sequence with randomly generated binary bits and the fixed length is transmitted through it. The weighting coefficients of each DFE are optimised during the training process and fixed after reaching their optimal values. Then, the real data can be processed by well-trained DFEs.

E. Angular Diversity Receiver Design

Fig. 5 presents the structure of an angular diversity receiver, which consists of seven REs pointing in different directions. Such a receiver was implemented in the hOME Gigabit Access project (OMEGA) [30].

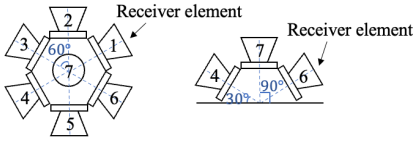

Fig. 5. Geometry of the receiver: Top view (left), and front view (right).

Each RE includes an optical filter, a non-imaging concentrator to collect the optical signal, a photodetector to convert optical power to an electrical signal, and a pre-amplifier to amplify the signal [31]. The collection area and the half-angle FOV of each RE are given in Table I. The half-angle FOV is set as 33°, constraining the number of transmitted signals received by each RE and mitigating multi-stream interference (MSI). The modelling assumes that the REs is located at the same point but at different angles.

III. Adaptive MIMO-VLC System

A. Data Rate-Adaptive Modulation

An indoor MIMO-VLC system typically has the same data rate for all channels, such as the system in [24]. However, a channel (or channel group) with higher SINR can achieve a higher data rate than other channels (under the same BER requirement). The system can obtain the optimised data rate performance when channels with different conditions adapt to their maximum data rates. However, the bit transitions of these waveforms will become misaligned as data rates vary. In this case, the time-alignment of waveforms can be done for simplicity of processing.

A data rate-adaptive modulation technique is implemented to ensure the time-alignment of the waveforms [14]. This time-alignment is achieved by controlling the up-sampling factor (U_f) of each channel according to its desired data rate. Fig. 6 is a simple schematic presenting the mechanism of this technique. Two signal waveforms from different sources have the same sample period T_{sample} and packet duration t_{packet}. If the data rate of waveform 2 is twice as fast as waveform 1, the number of the up-sampling factors of waveform 1 needs to be two times larger than waveform 2. Under this condition, the samples of different waveforms become time-aligned at every time instant during the packet time.

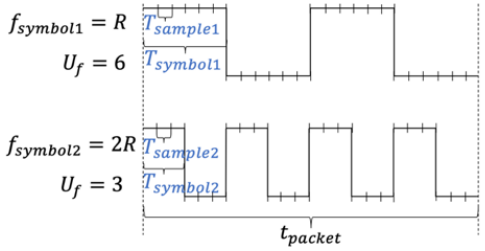

Fig. 6. Schematic of the data rate adaptive technique.

The maximum and minimum values of the up-sampling factors should be chosen, ensuring the numbers of samples per bit and the available up-sampling factor range are sufficient. After this, the number of symbols per packet duration (N_{symbol}) and the data rates (f_{symbol}) can be calculated from them

$$N_{symbol} = \frac{N_{sample}}{U_f} = \frac{t_{packet}}{T_{sample} \times U_f}, \tag{15}$$

where N_{sample} is the number of samples, T_{sample} is the sample period, t_{packet} is the packet duration.

The data rate is calculated as

$$f_{symbol} = \frac{1}{T_{symbol}} = \frac{1}{T_{sample} \times U_f}. \tag{16}$$

where T_{symbol} is the symbol period.

Equations (15) and (16) show that the maximum and minimum up-sampling factors, available data rate range and the packet duration are jointly decided.

B. Transmitter Coordination Algorithm

Section I mentions that the commonly used schemes of the MIMO-VLC system include spatial multiplexing (SMP), ganging and spatial modulation (SM). Here, an algorithm called the Channel Condition-based Transmitter Coordination (CCTC) algorithm is implemented. The CCTC algorithm adaptively combines SMP and ganging and employs data rate-adaptive modulation to improve the overall data rate of the system jointly. The overall data rate is the total data rate of all available channel groups.

There are two stages in the CCTC algorithm. At stage (1), the CCTC algorithm coordinates the channels to one or several group(s) based on their conditions. When the channel matrix is well-conditioned, SMP can be applied to transmit different data sequences and achieve a high overall data rate. When some channels suffer from high multi-stream interference (MSI) between them or have low SINR, the algorithm will convert to partial or full ganging to drive these channels to transmit the same data together. At stage (2), the data rate of each channel group is maximised using data rate-adaptive modulation.

Fig. 7 shows all the potential CCTC transmitter patterns with different channel groupings. Each small square represents a LED, with colour showing its pattern group. Pattern 1 denotes SMP, pattern 2 indicates partial ganging with three different data sequences delivered, pattern 3 indicates partial ganging with two different data sequences transmitted, and pattern 4 is full ganging.

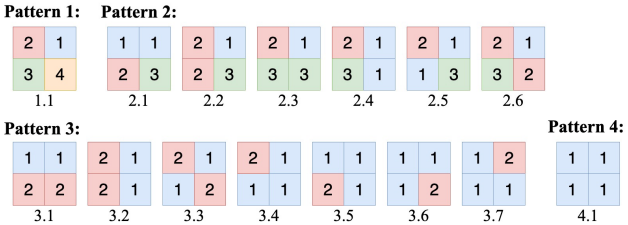

Fig. 7. Channel condition-based transmitter coordination patterns.

Algorithm 1 shows the details of the CCTC algorithm [14]. At each receiver position, the CCTC algorithm determines the applied scheme (SMP, partial ganging or full ganging) according to the initial BER values. After that, the data rate of each channel group is decided by adjusting the value of the up-sampling factor.

Algorithm 1 Transmitter operation to achieve maximum data rate with BER $\leq 1 \times 10^{-3}$

Initialisation: Denote $\boldsymbol{U}_f$ as the vector temporarily stores the up-sampling factors of 1 to N_t LEDs, the number of channels is $c \leftarrow 4$ and pattern number is $pt^{(c)} \leftarrow 1$;
$\boldsymbol{d} = [0\ 0\ 0\ 0]$;
while $c >= 1$, **do**
  At the specific receiver location (p_1, p_2), calculate $BER^{(c,pt)}$ of each channel and $BER_{overall}^{(c,pt)}$ average through channels;
  if $BER_{overall}^{(c,pt)} \leq 1 \times 10^{-3}$ **then**
    if $BER^{(c,pt)}$ of each channel $\leq 1 \times 10^{-3}$ while achieves the lowest $\boldsymbol{U}_f$ **then**
      Store $\boldsymbol{U}_f$ and corresponding data rates $\boldsymbol{R_b}$ for receiver location (p_1, p_2):
      for row = 1:c **do**
        $\boldsymbol{U}(p_1, p_2, row) = \boldsymbol{U}_f(row)$;
        $\boldsymbol{R}(p_1, p_2, row) = \boldsymbol{R_b}(row)$;
        $\boldsymbol{R_{sum}}(p1, p2) = sum(\boldsymbol{R_b})$;
      end for
    end if
    for row = 1:c **do**
      if $BER^{(c,pt,row)} \leq 1 \times 10^{-3}$ **and** $\boldsymbol{U}_f \geq \boldsymbol{U}_l$ **and** $\boldsymbol{U}_f \leq \boldsymbol{U}_u$ **then**
        $\boldsymbol{U}_f(row) = \boldsymbol{U}_f(row) - 1$;
        $\boldsymbol{d}(row) = 1$;
      elseif $BER^{(c,pt,row)} > 1 \times 10^{-3}$ **or** $\boldsymbol{U}_f < \boldsymbol{U}_l$ **then**
        $\boldsymbol{U}_f(row) = \boldsymbol{U}_f(row) + 1$;
      elseif $BER^{(c,pt,row)} > 1 \times 10^{-3}$ **and** $\boldsymbol{d}(row) == 0$
        $\boldsymbol{U}_f(row) = \boldsymbol{U}_f(row) + 1$;
      end if
    end for
  elseif $BER_{overall}^{(c,pt)} \geq 1 \times 10^{-3}$ **and** $c > 1$ **then**
    $c \leftarrow c - 1$;
  elseif
    $\boldsymbol{U}(p_1, p_2) = NaN$;
    $\boldsymbol{R_{sum}}(p1, p2) = NaN$;
  end if
end while

In Algorithm 1, $\boldsymbol{U}_f$ is a vector with c elements that temporarily stores the values of the up-sampling factors. $\boldsymbol{U}_u$ and $\boldsymbol{U}_l$ are the upper and the lower bounds of the up-sampling factor range. $\boldsymbol{U}$ is a $p_1 \times p_2$ matrix storing the final values of up-sampling factors for all receiver positions across the room. $\boldsymbol{R}$ stores the optimal data rates of all channel groups. $\boldsymbol{R_{sum}}$ is a $p_1 \times p_2$ matrix saving the final overall data rate at each receiver position across the room.

C. MIMO Matrix Estimation Sensitivity

Reference [17] shows that the channel estimation errors are expected to be considered when the channel state information is not perfectly known. To decide whether channel estimation errors need to be taken into account, a limited tolerance analysis would launch in the proposed system to understand the sensitivity to the estimation of the MIMO matrix. The MIMO matrix coefficients are truncated to two decimal points in a new system. In the test, this system showed very similar

performance to the system with full accuracy coefficients, demonstrating the robustness of the proposed approach. This matches our expectations, as the decision-making about the optimal transmitter pattern is not fine-grained. The same transmitter pattern can be applied over a broad range of receiver positions (corresponding to a range of different channel matrices).

D. Performance Comparison

In the simulation, the up-sampling factor range is set from 6 to 20, and the corresponding data rates per channel are from 100 Mbps to 333.33 Mbps. The sampler duration is 0.5ns, and the packet duration t_{packet} is 0.1 ms. There are 50 data packets transmitted, and each packet has 200 thousand bits. The DFEs have 24 feedforward and 19 feedback filter taps. The training step size is 0.01. The training length is 400 thousand samples per user location (the training data occupies 2 data packets).

Fig. 8 shows the overall data rates for the system with the CCTC algorithm and SMP.

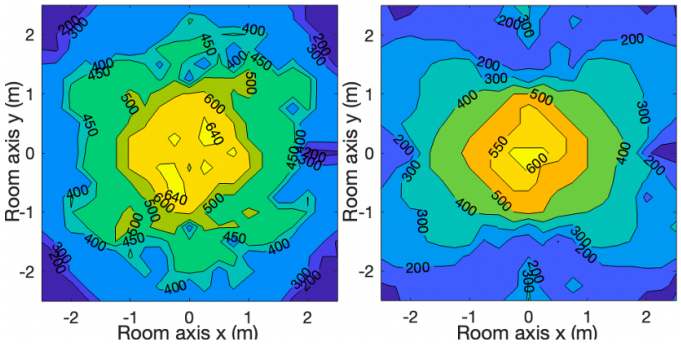

Fig. 8. Overall data rates for the system with the CCTC algorithm (left) and SMP (right).

The results show that the proposed techniques improve the overall data rate by 41 per cent on average than SMP. However, the CCTC algorithm still takes a large amount of computing time. Hence, a solution to further decrease the computational complexity of the proposed algorithm is investigated in the next section.

IV. Neural Network-Based MIMO-VLC System

A. Neural Network Settings

The CCTC algorithm has two stages, as mentioned in section III. The exhaustive search in each stage takes a significant amount of time. Hence, a neural network approach to reduce this is explored.

First, the neural network is employed to replace stage (1) of the CCTC algorithm and does not change stage (2). A feedforward multilayer perceptron (MLP) artificial neural network (ANN) is implemented, which is a commonly used network applicable to a variety of problems, such as non-linear prediction and pattern recognition [32]. Fig. 9 shows the architecture of the proposed network. The system is a two-layer feedforward network, including one input layer, one hidden layer and one output layer.

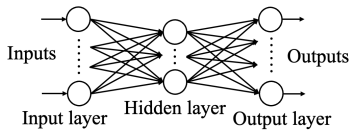

Fig. 9. Architecture of the MLP ANN.

The selection of the optimal transmitter pattern at stage (1) is a pattern recognition problem, which means the neural network identifies the target category of each input. The input of the neural network is the $N_r \times N_t$ MIMO matrix between the LEDs and the REs introduced in (2) in section 2. Hence the number of neurons in the input layer is set to $N_r \times N_t$. The input layer connects the hidden layer, and the activation function of the hidden layer is the sigmoid function. The output layer uses the softmax function. The output of the neural network is the transmitter pattern index. Therefore, the number of neurons in the output layer equals the number of transmitter pattern types. The output is evaluated by calculating the cross-entropy between the results obtained from the CCTC algorithm and the MLP ANN. Every neuron in the hidden layer and the output layer has weights from all the connected neurons in the previous layer and a bias value. The weights and biases are optimised when the cross-entropy is minimised using the gradient descent technique [18]. After that, the MLP ANN is well-trained and can be used to predict the optimal transmitter patterns.

B. Initial Tests

The constructed MLP ANN is employed to predict the optimal transmitter pattern with varying receiver positions relative to the LEDs, even with positions out of the range of the training data.

The number of neurons in the input layer is $N_r \times N_t = 28$. The hidden layer has 10 neurons. In the output layer, there are 15 neurons, matching the number of patterns given in Fig. 7. The MLP ANN system has two phases: a training phase and a testing phase. The training phase employs two rooms with sizes of 7 m × 7 m × 3 m (Room T_1) and 7 m × 7 m × 4.5 m (Room T_2). In each room, there are 225 channel matrices obtained from 225 (15 × 15) different user locations (picked from the receiver plane with a 0.5m array pitch). In sum, 450 channel matrices form the input set, and the corresponding 450 patterns calculated from the CCTC algorithm are the targets.

In the testing phase, three different room sizes are employed, as shown in Table II.

TABLE II
Room Types in Testing Phase

Room Type	Room Size	Testing Points	Array Pitch
A	4.5 m × 4.5 m × 3 m	10 × 10 = 100	0.5 m
B	6 m × 6 m × 5 m	7 × 7 = 49	1 m
C	8 m × 8 m × 2 m	9 × 9 = 81	1 m

If the patterns derived from the MLP ANN cannot meet the BER requirement at some user locations, the patterns are directly changed to full ganging at these locations.

Fig. 10 shows the mean aggregate data rates versus the receiver's distance to the room centre. The results obtained from the MLP ANN are compared to the results obtained from the CCTC algorithm. Each marked point on the plot is the mean of the data ±0.25m on either side of the distance from the room centre. Room A has the same height as Room T_1, with each

testing point set at the centroid of every four adjacent training points in Room T_1. Room B has a higher height than the rooms in the training phase. Room C has a shorter height but larger coverage area than the rooms in the training phase, which means the LED irradiance angles from the LEDs to user locations near the room corner of Room C are larger than those in the training set. The results obtained with the MLP ANN and the CCTC algorithm are in good agreement for all room types.

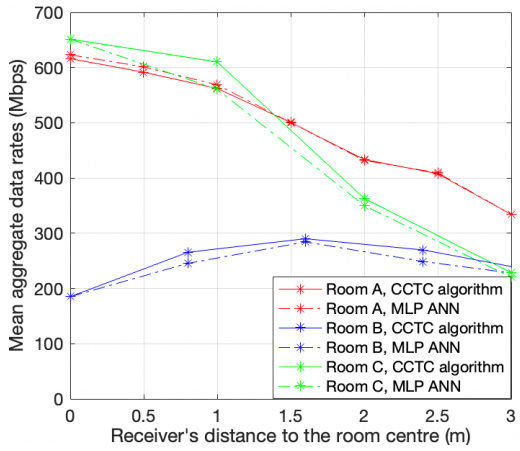

Fig. 10. Mean aggregate data rates versus receiver's distance to the room centre.

Results also show that the computing time using the MLP ANN is around four times faster than the CCTC algorithm in all three cases. The MLP ANN can efficiently predict the optimal transmitter pattern with a shorter computing time, even if the receiver position is outside the height and the coverage of the training set.

V. Receiver with Human Walking Activity Model

In this section, the MLP ANN is examined under practical scenarios. The ANN is trained using a data set that represents a range of possible receiver orientations and positions. To test the trained-ANN, we use a statistical model of a user walking within the coverage area with a mobile device whose orientation changes. The model is described below.

A. Receiver Orientation Model

In [33], an experiment was conducted (with 40 participants and 222 datasets) to develop a statistical model of the mobile device while the user is using it. This reference introduces an orientation-based random waypoint (ORWP) mobility model, which shows the random orientation and position of the receiver during the walking activities of the user. The ORWP model is introduced in this section to generate the testing data and examine the performance of the MLP ANN. This subsection details the orientation model of the receiver, and the following subsection provides the waypoint model.

First, Fig. 11 gives a schematic of the mobile device with the inbuilt angular diversity receiver. The schematic exhibits the pointing direction of each RE relative to the mobile device.

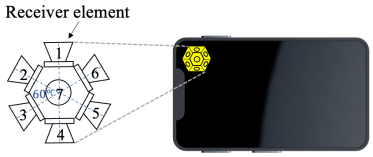

Fig. 11. Mobile device with the angular diversity receiver installed (receiver size not to scale).

Two coordinate systems are introduced to represent the orientation of the mobile device. Fig. 12(a) presents that the mobile device local coordinate system is defined with xyz, and the geographic coordinate system is presented with XYZ [33]. Fig. 12 shows the rotation of the mobile device around the x, y and z axes. The rotation angles are called yaw angle (ϕ_1), pitch angle (ϕ_2) and roll angle (ϕ_3) as shown in Fig. 12(b)-(d), respectively. The normal vector of the xy-plane of the mobile device is set as $\boldsymbol{n} = [n_1, n_2, n_3]^T$. The original direction is assumed as $\boldsymbol{n} = [0,0,1]^T$ in a cartesian coordinate system.

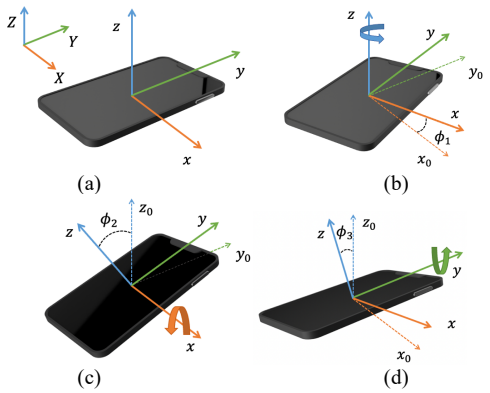

Fig. 12. Device orientation: (a) Original orientation, (b) Yaw rotation around the z-axis, with angle ϕ_1, (c) roll rotation around the y-axis, with angle ϕ_2, (d) pitch rotation around the x-axis, with angle ϕ_3. *Source: Redrawn from* [33].

To simplify the expressions hereinabove, the system is transferred to the spherical coordinate system. The polar angle θ is the angle between the normal vector $\boldsymbol{n}$ and the positive direction of the Z-axis. The azimuth angle φ is the angle between the projection of $\boldsymbol{n}$ on the XY-plane and the positive direction of the X-axis. Both angles are calculated using equations in [33].

The experiment in [33] shows that the polar angle's probability density function (PDF) θ follows a Gaussian distribution $\mathcal{N}(\mu, \sigma^2)$ with mean $\mu = 29.67°$ and standard deviation $\sigma = 7.78°$. The PDF of the azimuth angle φ shows a nearly uniform distribution $\varphi \sim \mathcal{U}[-\pi, \pi)$.

B. Orientation Random Waypoint Model of the Receiver

After getting the orientation model, the complete waypoint model is provided. In the ORWP model, users can walk inside the room with the mobile device held at the height of the receiver plane. Users pick the destination randomly within the indoor area and walk in a straight line from the start to the destination with a constant walking speed. There are a number of waypoints along this line, and each has different mobile device orientations.

The distance between two successive waypoints P_n and P_{n-1} ($n \in \mathbb{N}$) is the transition length $\mathcal{L}_n$. The transition lengths are

independent identically distributed (i.i.d.) random variables (RVs). The PDF of the RVs is given in [34]. In a $L \times L$ (width × length) squared room, the expected length of the RVs is $\mathbb{E}[\mathcal{L}] = 0.5214L$.

The experiment also shows that the adjacent samples in the random process are correlated. Hence, the polar angle θ is modelled as a correlated Gaussian random process with the details in [33].

C. Initial Up-Sampling Factor Prediction

In the initial tests, the neural network only substitutes stage (1) of the CCTC algorithm in section IV. In this section, other than the neural network employed in section IV, a second neural network is introduced to replace stage (2) of the CCTC algorithm to determine the initial up-sampling factor of each ganging channel group. Fig. 13 shows the relationship between two neural networks.

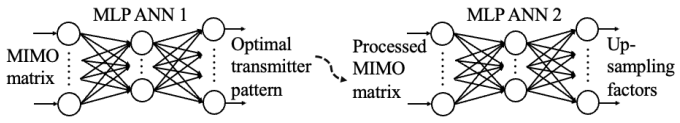

Fig. 13. Relationship between neural networks.

The input of the MLP ANN 2 is the processed MIMO matrix, which is calculated from the original MIMO matrix with the optimal transmitter pattern information obtained from the MLP ANN 1. The optimal transmitter pattern acquired from the MLP ANN 1 decides which columns in the original MIMO matrix could form a ganging group to transmit the same data stream. The input of the MLP ANN 2 is obtained by adding these ganging columns together and forming a new matrix. And to make sure the number of input neurons is a constant number $N_r \times N_t = 28$, zeros are added at the end of the new matrix.

The hidden layer of the MLP ANN 2 has ten neurons. The output layer has four neurons, representing the up-sampling factors of the corresponding channel groups, respectively. The last three values of the output neurons can be zeros when the system is partial or full ganging. For example, when there are three ganging groups, the last output of the MLP ANN 2 will be zero. If there are two ganging groups, the last two outputs will be zeros. If all four channels are ganged together, only one up-sampling factor is required, and the last three outputs will be zeros.

The up-sampling factor determination process is an input-output fitting problem, which means a mapping is required between a numeric input data set and a numeric output data set [35]. The MLP ANN 2 is a two-layer neural network. The hidden layer neurons use the sigmoid function, and the output neurons are linear. The Bayesian regularisation algorithm is selected as the training algorithm.

The up-sampling factors at the output are rounded to integers and used as the initial up-sampling factors at stage (2). Then, the CCTC algorithm is applied here to slightly adjust the final up-sampling factors to ensure the data rate of each channel group is maximised.

D. Performance Evaluation

The performance of the MLP ANN is evaluated based on the testing data obtained from the ORWP model (given in subsections A and B). The data rate performance across the room obtained with the MLP ANN is compared with the data rates obtained with the CCTC algorithm, the water-filling algorithm, full ganging and SMP. The water-filling algorithm is a benchmark of the MLP ANN approach, which achieves optimal power allocation for each channel in the MIMO system by maximising the system's capacity (see, e.g., [36]). The water-filling algorithm allows different data sequences to be transmitted at different power levels for each transmitter, while the MLP ANN fixes the modulated power at each transmitter and 'steers' data to different patterns of transmitters. Table III shows the parameters employed. The total transmitted power is 4W. The system with the water-filling algorithm possesses flexible power allocation among four LEDs while other systems have fixed power, 1W, for each LED. The system model is the same as the model in section II with parameters in Table I. Table IV presents the training data used to train the MLP ANN.

TABLE III
PARAMETERS

Parameters	Values
Room size (width × length × height)	6 m × 6 m × 3 m
Receiver plane height	1 m
User walking speed	2 m/s [12]
Number of movement periods in ORWP model (n)	341
Number of destinations in ORWP model (k)	30
Total power of four LEDs	4W

TABLE IV
TRAINING DATA SETS

Room Size	Azimuth Angle (φ)	Polar Angle (θ)	Array Pitch
7m × 7m × 3m	30°	0°	0.5m
	30°i with i = 0,1,2	30°	0.5m
	with i = 3,4,6,8,10		1m
7m × 7m × 2.5m	30°i with i = 0,1,2	30°	1m

Fig. 14 presents the mean aggregate data rate versus the receiver's distance to the room centre for the system using the MLP ANN, the CCTC algorithm, the water-filling algorithm, ganging and SMP.

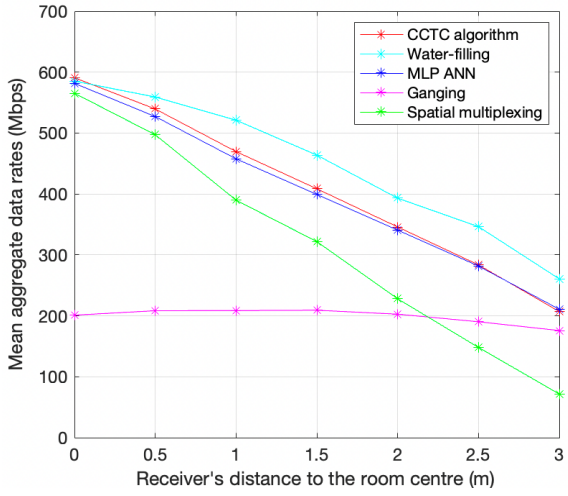

Fig. 14. Mean aggregate data rates versus distance to the room centre.

First, the performance of the MLP ANN is examined by comparing the result with that of the CCTC algorithm. The plots obtained with the MLP ANN and the CCTC algorithm is redrawn in Fig. 15. Fig. 15(a) presents the comparison of the

mean aggregate data rates, in which we can find that the MLP ANN works as good as the CCTC algorithm in obtaining the optimal transmitter pattern and the optimal mean aggregate data rates. Fig. 15(b) presents the difference histogram of the mean aggregate data rates between the two techniques. Most data are gathered around the zero-error line, with a minor amount of data spread out within a limited range, showing good agreement between the two approaches. The MLP ANN gives reliable performance and can replace the CCTC algorithm. Table V shows that the MLP ANN-based system is almost four times faster than the CCTC algorithm-based system.

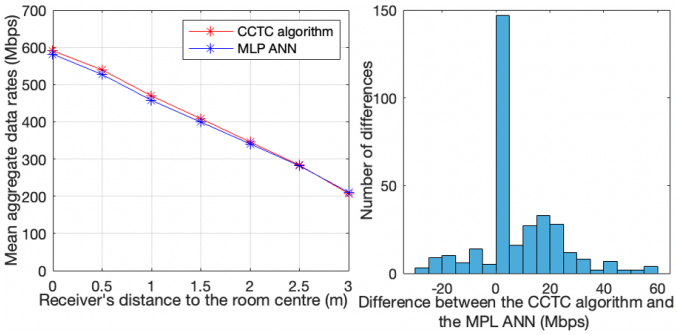

(a) (b)

Fig. 15. (a) Mean aggregate data rates comparison for the CCTC algorithm and the MLP ANN, (b) Difference histogram for the CCTC algorithm and the MLP ANN.

Second, the lines representing the systems with the MLP ANN, ganging and SMP are analysed. Fig. 14 shows that the MLP ANN achieves a much higher mean aggregate data rate than full ganging and SMP across the room. The reason is that the MLP ANN can switch between full ganging, partial ganging and SMP according to the channel condition to optimise the data rates. When the MIMO matrix is ill-conditioned at the room corner, the MLP ANN uses a ganging scheme to group all the channels to transmit the same data, minimising multi-stream interference (MSI) between different channels. When the channel conditions improve from the room corner to the room centre, the system can adaptively switch to partial ganging or pure SMP to replace the full ganging approach and achieve a higher data rate.

Third, the MLP ANN is compared to its benchmark, the water-filling algorithm. Fig. 16(a) shows the mean aggregate data rates for the system using the MLP ANN and the water-filling approach. The bars represent the spread of the values for a particular distance from the room centre and represent one standard deviation (one-sigma) from the mean value of the data rate for this distance. The water-filling algorithm gives higher mean aggregate data rates, especially when the receiver's distance to the room centre is larger than 1m. The MLP ANN also shows a more significant variation in data rates than the water-filling algorithm in the middle of the room.

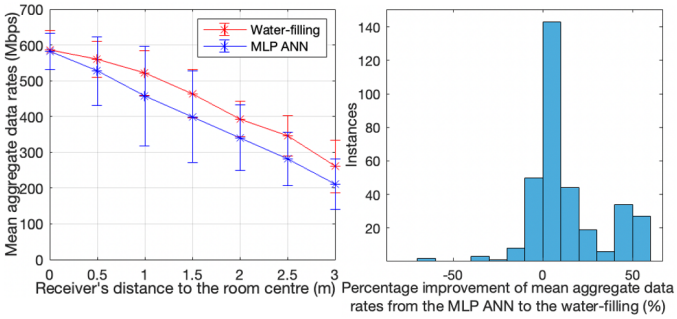

(a) (b)

Fig. 16. (a) Mean aggregate data rates for the water-filling algorithm and the MLP ANN with the bar, (b) Difference histogram for the water-filling algorithm and the MLP ANN.

Fig. 16(b) presents the normalised difference histogram of the mean aggregate data rates between the MLP ANN and the water-filling algorithm. The normalised difference is calculated as the measure of the percentage reduction of the MLP ANN approach's data rate performance compared with the water-filling algorithm. After the calculation, the MLP ANN has an average of 12 per cent lower data rate when compared with the water-filling algorithm.

Although the MLP ANN has a reduction in the data rate, it has advantages compared with the water-filling algorithm in several aspects:

1) Computing Time

Table V gives the computing time comparison of the CCTC, water-filling and MLP ANN approaches. The computing time of the MLP ANN-based system is more than three times faster than that of the water-filling algorithm-based system and the CCTC algorithm-based system.

TABLE V
COMPUTING TIME AND DATA RATE COMPARISON

Approach	Computing Time	Average Data Rate
CCTC	1.278×10^5 s = 35.49 h	404.9 Mbps
Water Filling	1.089×10^5 s = 30.24 h	448.99 Mbps
Neural Network	3.528×10^4 s = 9.78 h	397.35 Mbps

The number of floating-point operations (FLOPs) of the system is another measurement of the system's complexity. The MLP ANN-based system has around 1.45×10^{11} FLOPs, and the CCTC algorithm-based system has 7.67×10^{11} FLOPs. The number of flops of the CCTC algorithm-based system is five times greater than that of the MLP ANN-based system. The ratio obtained from the computing time roughly corresponds to the ratio obtained from the number of FLOPs.

2) Lighting Sources

The MLP ANN-based system only moves data around the luminaires which are driven at constant modulation current. The water-filling algorithm-based system has flexible power levels, requiring a more complex controller for the sources.

3) Illumination

The MLP ANN-based system offers stable illumination. The water-filling algorithm concentrates all the power to one or two LED(s) when needed. The unbalanced power distribution among LEDs may cause a dimming and colour inconsistency issue [37].

In summary, there is a trade-off between the MLP ANN and the water-filling approach. The MLP ANN is demonstrated as

a fast and simple alternative for the complex water-filling algorithm.

VI. Conclusion

In this paper, we have investigated MLP ANN-based MIMO-VLC systems with transmitter pattern and data rate coordination. The new system has the following advantages: (1) The ANN-based system considers statistical models with different room geometries, receiver positions and orientations. ANNs is robust and performs well even the testing data falls outside the scope of the training data. (2) The computational complexity of the ANN-based system is four times lower than the CCTC algorithm-based one and three times lower than the water-filling algorithm. (3) The implementation and control of the ANN-based system are more straightforward than that of the water-filling algorithm. Future work in this area will focus on: (1) Simplifying the channel selection process. (2) Incorporating other capabilities such as beam-steering into the system to further improve the data rate performance. (3) Developing the algorithm to make it adapt to multi-user scenarios. Different channel access methods, handover between different channels and the method to prevent interference in the overlapping area will be considered.

References

[1] G. Staple and K. Werbach, "The end of spectrum scarcity," *IEEE Spectr.*, vol. 41, no. 3, pp. 48–52, Mar. 2004.

[2] K. D. Dambul, D. C. O'Brien, and G. Faulkner, "Indoor optical wireless MIMO system with an imaging receiver," *IEEE Photon. Technol. Lett.*, vol. 23, no. 2, pp. 97–99, Jan. 2011.

[3] J. Lian and M. Brandt-Pearce, "Multiuser MIMO indoor visible light communication system using spatial multiplexing," *J. Lightwave Technol.*, vol. 35, no. 23, pp. 5024–5033, Dec. 2017.

[4] E. Poves, W. Popoola, H. Haas, J. Thompson, and D. Cárdenas, "Experimental results on the performance of optical spatial modulation systems," in *Proc. IEEE Veh. Technol. Conf. Fall*, Quebec City, QC, Canada, 2012, pp. 1–5.

[5] N. Ishikawa and S. Sugiura, "Maximizing constrained capacity of power-imbalanced optical wireless MIMO communications using spatial modulation," *J. Lightwave Technol.*, vol. 33, no. 2, pp. 519–527, Jan. 2015.

[6] W. Popoola, E. Poves, and H. Haas, "Generalised space shift keying for visible light communications," in *Proc. Int. Symp. CSNDSP*, Poznan, Poland, 2012, pp. 1–4.

[7] T. Fath and H. Haas, "Performance comparison of MIMO techniques for optical wireless communications in indoor environments," *IEEE Trans. Commun.*, vol. 61, no. 2, pp. 733–742, Feb. 2013.

[8] R. Mulyawan *et al.*, "MIMO visible light communications using a wide field-of-view fluorescent concentrator," *IEEE Photon. Technol. Lett.*, vol. 29, no. 3, pp. 306–309, Feb. 2017.

[9] S. Collins, D. C. O'Brien, and A. Watt, "High gain, wide field of view concentrator for optical communications," *Opt. Lett.*, vol. 39, no. 7, pp. 1756–1759, Apr. 2014.

[10] J. M. Kahn and J. R. Barry, "Wireless infrared communications," *Proc. IEEE*, vol. 85, no. 2, pp. 265–298, Feb. 1997.

[11] A. Nuwanpriya, S. W. Ho, and C. S. Chen, "Indoor MIMO visible light communications: Novel angle diversity receivers for mobile users," *IEEE J. Sel. Areas Commun.*, vol. 33, no. 9, pp. 1780–1792, Sep. 2015.

[12] J. B. Carruther and J. M. Kahn, "Angle diversity for nondirected wireless infrared communication," *IEEE Trans. Commun.*, vol. 48, no. 6, pp. 960–969, Jun. 2000.

[13] T. Q. Wang, C. He, and J. Armstrong, "Angular diversity for indoor MIMO optical wireless communications," in *Proc. IEEE Int. Conf. Commun.*, London, U.K., 2015, pp. 5066–5071.

[14] F. Dong, R. Singh, and D. O'Brien, "Adaptive MIMO-VLC system for high data rate communications," in *Proc. Globecom Workshops*, Taipei, Taiwan, 2020, pp. 1–6.

[15] A. Petroni, G. Scarano, R. Cusani, and M. Biagi, "Modulation Precoding for MISO Visible Light Communications," *J. Lightwave Technol.*, vol. 39, no. 17, pp. 5439–5448, Sep. 2021.

[16] X. Guo and N. Chi, "Superposed 32QAM Constellation Design for 2 × 2 Spatial Multiplexing MIMO VLC Systems," *J. Lightwave Technol.*, vol. 38, no. 7, pp. 1702–1711, Apr. 2020.

[17] K. Ying, H. Qian, R. J. Baxley, and S. Yao, "Joint Optimization of Precoder and Equalizer in MIMO VLC Systems," *IEEE J. Select. Areas Commun,*, vol. 33, no. 9, pp. 1949–1958, Sep. 2015.

[18] S. Bhama and H. Singh, "Single layer neural networks for linear system identification using gradient descent technique," *IEEE Trans. Neural Netw.*, vol. 4, no. 5, pp. 884–888, Sep. 1993.

[19] W. Sayed, T. Ismail, and K. Elsayed, "A neural network-based VLC indoor positioning system for moving users," in *Proc. Intl. Conf. Smart Apl., Commun. Netw.,* Sharm El Sheik, Egypt, 2019, pp. 1–5.

[20] J. He *et al.*, "Demonstration of high precision 3D indoor positioning system based on two-layer ANN machine learning technique," in *Proc. Opt. Fiber Commun. Conf.*, San Diego, California, 2019, pp. 1–3.

[21] S. A. I. Alfarozi, K. Pasupa, H. Hashizume, K. Woraratpanya, and M. Sugimoto, "Robust and unified VLC decoding system for square wave quadrature amplitude modulation using deep learning approach," *IEEE Access*, vol. 7, pp. 163262–163276, 2019.

[22] S. Ma *et al.*, "Signal demodulation with machine learning methods for physical layer visible light communications: Prototype Platform, Open Dataset, and Algorithms," *IEEE Access*, vol. 7, pp. 30588–30598, 2019.

[23] S. Rajbhandari *et al.*, "Neural network-based joint spatial and temporal equalization for MIMO-VLC system," *IEEE Photon. Technol. Lett.*, vol. 31, no. 11, pp. 821–824, Jun. 2019.

[24] L. Zeng *et al.*, "High data rate multiple input multiple output (MIMO) optical wireless communications using white LED lighting," *IEEE J. Sel. Areas Commun.*, vol. 27, no. 9, pp. 1654–1662, Dec. 2009.

[25] A. Moreira, R. Valadas, and A. M. De Oliveira Duarte, "Optical interference produced by artificial light," *Wireless Networks*, vol. 3, pp. 131–140, May 1997.

[26] H. Le Minh *et al.*, "High-speed visible light communications using multiple-resonant equalization," *IEEE Photon. Technol. Lett.*, vol. 20, no. 14, pp. 1243–1245, Jul. 2008.

[27] L. Zeng, D. O'Brien, H. Le-Minh, K. Lee, D. Jung, and Y. Oh, "Improvement of date rate by using equalization in an indoor visible light communication system," in *Proc. IEEE ICCSC*, Shanghai, China, 2008, pp. 678–682.

[28] D. C. O'Brien and M. Katz, "Optical wireless communications within fourth-generation wireless systems [Invited]," *J. Opt. Netw.*, vol. 4, no. 6, pp. 312–322, Jun. 2005.

[29] A. Goldsmith, *Wireless Communications.* Cambridge, U.K.: Cambridge Univ. Press, 2005, pp. 338–340.

[30] J.-P. Javaudin, M. Bellec, D. Varoutas, and V. Suraci, "OMEGA ICT project: Towards convergent gigabit gome networks," in *Proc. IEEE Intl. Symp. Personal, Indoor Mobile Radio Commun.*, Cannes, France, 2008, pp. 1–5.

[31] A. Jovicic, J. Li, and T. Richardson, "Visible light communication: Opportunities, challenges and the path to market," *IEEE Commun. Mag.*, vol. 51, no. 12, pp. 26–32, Dec. 2013.

[32] S. Agatonovic-Kustrin and R. Beresford, "Basic concepts of artificial neural network (ANN) modeling and its application in pharmaceutical research," *J. Pharm. Biomed. Anal.*, vol. 22, no. 5, pp. 717–727, Jun. 2000.

[33] M. D. Soltani, A. A. Purwita, Z. Zeng, H. Haas, and M. Safari, "Modeling the random orientation of mobile devices: Measurement, analysis and LiFi use case," *IEEE Trans. Commun.*, vol. 67, no. 3, pp. 2157–2172, Mar. 2019.

[34] C. Bettstetter, H. Hartenstein, and X. Costa-Pérez, "Stochastic properties of the random waypoint mobility model," *Wireless Networks*, vol. 10, pp. 555–567, 2004.

[35] M. Chen, U. Challita, W. Saad, C. Yin, and M. Debbah, "Artificial neural networks-based machine learning for wireless networks: A tutorial," *IEEE Commun. Surv. Tutorials*, vol. 21, no. 4, pp. 3039–3071, 2019.

[36] J. M. Cioffi, "Multi-channel modulation," in *Advanced Digital Communications*. Stanford, CA, USA: Stanford Univ., 2014, ch. 4. [Online]. Available: https://web.stanford.edu/class/ee379c/readerfiles/chap4.pdf

[37] A. T. L. Lee, H. Chen, and S.-C. Tan, "Precise dimming and color control of LED systems based on color mixing," *IEEE Trans. Power Electron.*, vol. 31, no. 1, pp. 65–80, Jan. 2016.